PCCP

New insights into band inversion and topological phase of TiNI monolayer

Complete List of Authors:	Yalameha, Shahram; University of Isfahan, Department of Physics Nourbakhsh, Zahra; University of Isfahan Bahramy, Mohammad Saeed; University of Manchester, Department of Physics and Astronomy Vashaee, Daryoosh; North Carolina State University, Department of Electrical and Computer Engineering; North Carolina State University, Department of Materials Science and Engineering

Yalameha *et al.*

New insights into band inversion and topological phase of TiNI monolayer

Shahram Yalameha [1], Zahra Nourbakhsh [1], Mohammad Saeed Bahramy [2], and Daryoosh Vashaee [3,4,1]

[1]*Faculty of Physics, University of Isfahan, 81746-73441, Isfahan, Iran*
[2]*Department of Physics and Astronomy, University of Manchester, Oxford Road, Manchester M13 9PL, UK.*
[3]*Department of Electrical and Computer Engineering, North Carolina State University, Raleigh, NC 27606, USA*
[4]*Department of Materials Science and Engineering, North Carolina State University, Raleigh, NC 27606, USA*

Two-dimensional (2D) topological insulators (TIs) hold great promise for future quantum information technologies. Among the 2D-TIs, the TiNI monolayer has recently been proposed as an ideal material for achieving the quantum spin Hall effect at room temperature. Theoretical predictions suggest a sizable bandgap due to the spin-orbit coupling (SOC) of the electrons at and near the Fermi level with a nontrivial $\mathbb{Z}2$ topology of the electronic states, which is robust under external strain. However, our detailed first-principles calculations reveal that, in contrast to these predictions, the TiNI monolayer has a trivial bandgap in the equilibrium state with no band inversion, despite SOC opening the bandgap. Moreover, we show that electron correlation effects significantly impact the topological and structural stabilities of the system under external strains. We employed a range of density functional theory (DFT) approaches, including HSE06, PBE0, TB-mBJ, and GGA+U, to comprehensively investigate the nontrivial topological properties of this monolayer. Our results demonstrate that using general-purpose functionals such as PBE-GGA for studying TIs can lead to false predictions, potentially misleading experimentalists in their efforts to discover new TIs.

I. INTRODUCTION

Two-dimensional (2D) quantum materials such as 2D topological insulators (TIs) and 2D topological Dirac semimetals have become a new paradigm in condensed matter physics because of their exotic properties and technological applications in spintronics and quantum computing [1-6]. The quantum spin Hall (QSH) insulators, known as 2D TIs, host an insulating bulk gap and unique edge states that are protected by time-reversal symmetry (TRS) [3, 7-9]. In addition to 2D TIs, another class of 2D quantum materials is 2D topological Dirac semimetals. Graphene is the first and most obvious example of 2D Dirac materials [10]. The Dirac points of graphene are located at *K* and *K'* high symmetry points. These Dirac points are protected by inversion, and time-reversal symmetry, where the spin rotation symmetry is conserved. Generally, a 2D Dirac semimetal can be located at high symmetry points, along high symmetry lines, or generic points in the 2D Brillouin zone (BZ). For example, NP [11], Ta_2Se_3 [12], Be_3C_2 [13], and B_2S [14] 2D materials have such Dirac points.

The key identifiers of 2D/3D TIs are band inversion and topological invariants [2]. Theoretically predicted and experimentally observed TIs usually appear in those materials containing elements with strong SOC [15, 16]. Although band inversion cannot rigorously define any topological phase, it is very suggestive in identifying compounds for new topological states and understanding the topological nature of various topological materials [17]. The SOC may induce a band inversion, changing the band gap in TIs [1]. It should be noted that band inversion

---

[1] Email: dvashae@ncsu.edu

Yalameha *et al.*

occurs at points in the BZ called time-reversal invariant momentum (TRIM) points [3, 18]. The TRIMs are the points in reciprocal space connected via a reciprocal lattice vector and a time-reversal (TR) operation. In bulk materials, these TRIMs Γ_i are defined by $-\Gamma_i = \Gamma_i + \mathbf{G}$, where $\mathbf{G}$ is a bulk reciprocal transfer lattice vector. The Γ point in the bulk BZ is thus always a TRIM. There are seven (three) more possibilities in 3D (2D) that can be found using the reciprocal lattice vector $\mathbf{G} = m\mathbf{b}_1 + n\mathbf{b}_2 + o\mathbf{b}_3$ (m, n, and o are 0 or 1). The TRIMs are the points on the BZ boundary reached by moving halfway along these vectors. The specific TRIMs depend on the crystal structure. The high symmetry of the TRIMs is reflected in the symmetry of the electronic band structure. Suppose that we have an electronic state with energy and spin $\epsilon^{\uparrow}(\boldsymbol{k})$. Kramer's degeneracy guarantees the existence of a degenerate state $\epsilon^{\downarrow}(-\boldsymbol{k})$. If $\boldsymbol{k}$ is a TRIM, $-\boldsymbol{k}$ can also be reached by adding a reciprocal lattice vector to $\boldsymbol{k}$, implying that there must not only be a degenerate state $\epsilon^{\downarrow}(-\boldsymbol{k})$ but also one $\epsilon^{\uparrow}(\boldsymbol{k})$, that is, the state is double-degenerate at a TRIM [19]. Interestingly, for materials with inversion symmetry, this does not have any consequences because the inversion symmetry alone guarantees the bands spin degeneracy, as it implies the existence of a state $\epsilon^{\uparrow}(-\boldsymbol{k})$ for every state $\epsilon^{\uparrow}(\boldsymbol{k})$ in the BZ [19]. Another key identifier is nontrivial edge/surface states protected by TRS due to the double degeneracy guaranteed by Kramers' theorem [2, 18]. The Berry curvature is closely related to many physical phenomena, leading to nontrivial edge/surface states showing unique electronic transport properties [2, 20]. The unique aspect of topological insulators is the robust, spin-polarized conducting surface state encapsulating these materials. The topological surface state can serve as a platform to study fundamental quasiparticle phenomena such as *Majorana* fermions [21] and magnetic monopole-like behavior [22], as well as to explore future electronics such as quantum computing and spintronics [23, 24].

Recently, a new class of layered transition metal nitride halides (MTiX, M = Zr, Hf; X = Cl, Br, I) and their monolayer phase have been experimentally and theoretically investigated [25-28]. Moreover, Liang *et al.* [26] and Wang *et al.* [29] have proposed titanium nitride halides monolayers (TiNX; X = F, Cl, Br, I), which are dynamically and thermally stable, and their optical, transport, and thermoelectric properties have been extensively investigated. Most recently, Wang *et al.* [28] found that the TiNI monolayer possesses nontrivial topological properties. This monolayer is predicted to undergo a band inversion at the Γ point within the Perdew–Burke–Ernzerhof generalized gradient approximation (PBE-GGA). The origin of this band inversion has, however, not been determined. The resulting bandgap is suggested to be 50.7 meV along the Γ-X direction in the Brillouin zone. Furthermore, including electron correlation effects within the HSE06 formalism seems to further increase the nontrivial bandgap to 273.1 meV, suggesting that the QSH effect can be easily achieved at room temperature due to this small energy bandgap.

One of the challenges before entering the stage of experimental investigations, especially in two-dimensional materials, is the correct detection and evaluation of the bandgap and the stability of the compounds, which can be done using the first-principles calculations. We revisit the TiNI monolayer in the present work and study its topological properties. First, using the PBE-GGA approach, we study the topological properties, including band inversion, topological index $\mathbb{Z}_2$ by the Wilson-loop method [30], and topological edge states in the presence and absence of SOC. Next, we show that the band inversion in this monolayer is driven by the chemical bonding effect and not due to the spin-orbit coupling, a feature not realized before [28]. The findings from

Yalameha *et al.*

our investigation demonstrate that the TiNI monolayer does not possess a nontrivial bandgap in its equilibrium state, contrary to a prior report. The HSE06 and PBE0 hybrid functionals, as well as the TB-mBJ approach, were employed to reach this conclusion. Moreover, we analyzed the impact of uniaxial strain on the electronic properties of the TiNI monolayer and showed that it is insufficiently dynamically stable to support nontrivial topological states.

This paper is arranged as follows. In Sec. II, we briefly introduce the simulation methods. In Sec. III. A, we present the structural properties of the TiNI monolayer in comparison to other works. Sec. III. B is devoted to the numerical results, focusing on the electronic and topological properties of this monolayer. Finally, the conclusions of this work are highlighted in Sec. IV.

II. Computational Methods

We performed electronic band structure calculations of the TiNI monolayer using the density functional theory (DFT) implemented in the WIEN2K package [31]. The calculations were carried out using the Perdew-Burke-Ernzerhof (PBE) functional [32], as well as the Heyd-Scuseria-Ernzerhof (HSE06) [33] and PBE0 [34] hybrid functionals. To account for the strong correlation of the Ti element with [Ar] $3d^2 4s^2$ electron configuration and improve band splitting, we also applied the GGA+U method. In the GGA+U approach, we set the Hubbard U term for Ti to 1.2 eV, which resulted in calculated lattice parameters (a = 3.986 Å, b = 3.542 Å, c = 9.065 Å) of the TiNI bulk structure that are in good agreement with experimental values (a = 3.941 Å, b = 3.515 Å, c =8.955 Å) [35]. This value of the Hubbard U parameter is consistent with the value (1.0 eV) calculated by Wang et al. [28]. We also employed the Tran-Blaha modified Becke-Johnson exchange potential approximation (TB-mBJ) [36] calculations to improve the band gaps.

An 18×18×4 $\boldsymbol{k}$-point mesh is used in these calculations. A vacuum spacing of 15 Å between the neighboring slabs was applied to avoid unphysical interactions between periodic images. The edge states spectrums were calculated using the iterative Green's function method [37] in a tight-binding Hamiltonian based on the maximally localized Wannier functions projected from the bulk Bloch wave functions [38, 39]. In this method for the evolution of the Wannier Center of Charges (WCCs) for a given energy band *n*, we use the relationship between the Wannier functions (WFs) and lattice vector *R,* which can be written as:

$$|\boldsymbol{R}, n\rangle = \frac{1}{2\pi} \int_{-\pi}^{\pi} d\boldsymbol{k}\, e^{-i\boldsymbol{k}.(\boldsymbol{R}-x)} |u_{nk}\rangle. \qquad (1)$$

So, the WCC (i.e., $\bar{x}_n$) is defined as the mean value of $\langle 0n|\bar{x}|0n\rangle$, where $\bar{x}$ is the position operator, and $\langle 0n|$ is the state corresponding to a Wannier function in the cell with $R = 0$. Therefore, we can write [38-40],

$$\bar{x}_n = \frac{i}{2\pi} \int_{-\pi}^{\pi} dk\, \langle u_{nk}|\partial_k|u_{nk}\rangle \qquad (2)$$

Assuming that $\sum_i \bar{x}_i^I + \bar{x}_i^{II} = 1/2\pi \int_{BZ} A^I + A^{II}$ for Kramers pairs I and II, the summation is over the occupied states and $A\ (= A^I + A^{II})$ is the Berry connection. So, we have the formula for the $\mathbb{Z}_2$ topological index [40]:

$$\mathbb{Z}_2 = \sum_i [\bar{x}_i^I(T/2) - \bar{x}_i^{II}(T/2)] - \sum_i [\bar{x}_i^I(0) - \bar{x}_i^{II}(0)]. \qquad (3)$$

Yalameha *et al.*

Where T can be substituted for the k points of the first BZ. The $\mathbb{Z}_2$ topological index can be determined by the even or odd number of crossings of any arbitrary horizontal reference line [30, 41].

The phonon dispersion was calculated using the supercell approach with the finite displacement method. A $3\times3\times1$ supercell was built to calculate phonon dispersion using the PHONOPY package [42]. To investigate the interatomic bonding in the TiNI monolayer, we calculated the crystal orbital Hamiltonian populations (COHPs) using the LOBSTER package [43].

In this study, we utilized uniaxial strains to investigate the band structure and topological band order of the TiNI monolayer. To achieve this, in-plane uniaxial strains were applied along the x- and y-axis by uniformly altering the lattice with $\varepsilon = (l\text{-}l_0)/l_0$, where l (l_0) represents the strained (equilibrium) lattice constants ($l = a, b$). The two Bravais primitive lattice vectors were given by Eq. (4) and the reciprocal lattice basis vectors were calculated accordingly, as shown in Eq. (5).

$$\boldsymbol{R}_1 = (a, 0, 0), \boldsymbol{R}_2 = (0, b, 0), \qquad (4)$$

$$\boldsymbol{K}_1 = \frac{2\pi}{a}(1,0,0), \boldsymbol{K}_2 = \frac{2\pi}{b}(0,1,0), \qquad (5)$$

The TiNI Brillouin zone (BZ) is rectangular and contains four high-symmetry points, $\Gamma=(0, 0, 0)$, $X=(\pi/2a, 0, 0)$, $M=(\pi/2a, \pi/2b, 0)$, and $Y=(0, \pi/2b, 0)$, as shown in Fig. 1(b). Applying strain causes a change in the bond lengths of atoms. In the long wavelength region, the atom located at position r_1 is displaced to a new position, $r_2 = r_1 + r_1.\nabla u$, after the strain is applied. For a homogeneous strain, ∇u can be expressed as $\nabla u = \varepsilon$, where ε is the strain tensor. In the case of x-directed (y-directed) strain, the non-vanishing element of the strain tensor is ε_{xx} (ε_{yy}), denoted by ε_x or ε_y in the current literature for simplicity. Therefore, the two Bravais primitive lattice vectors can be expressed as shown in Eq. (6), and the reciprocal lattice basis vectors can be calculated immediately, as given in Eq. (7).

$$\boldsymbol{R}'_1 = ((1 + \varepsilon_{xx})a, 0, 0); \boldsymbol{R}'_2 = (0, b, 0)\text{:x-direction},$$
$$\boldsymbol{R}'_1 = (a, 0, 0); \boldsymbol{R}'_2 = (0, (1 + \varepsilon_{yy})b, 0)\text{:y-direction}, \qquad (6)$$

$$\boldsymbol{K}'_1 = \frac{2\pi}{a(1 + \varepsilon_{xx})}(1,0,0), \boldsymbol{K}'_2 = \frac{2\pi}{b}(0,1,0)\text{:x-direction},$$
$$\boldsymbol{K}'_1 = \frac{2\pi}{a}(1,0,0), \boldsymbol{K}'_2 = \frac{2\pi}{b(1+\varepsilon_{yy})}(0,1,0)\text{:y-direction}, \qquad (7)$$

As a result, the perfect rectangular BZ is deformed, and its coordinates are altered according to Eq. (8):

$$\Gamma = (0, 0, 0), X = \left(\frac{\pi}{2a(1+\varepsilon_{xx})}, 0, 0\right), M = \left(\frac{\pi}{2a(1+\varepsilon_{xx})}, \frac{\pi}{2b}, 0\right), Y = \left(0, \frac{\pi}{2b}, 0\right)\text{:x-direction}$$
$$\Gamma = (0, 0, 0), X = \left(\frac{\pi}{2a}, 0, 0\right), M = \left(\frac{\pi}{2a}, \frac{\pi}{2b(1+\varepsilon_{yy})}, 0\right), Y = \left(0, \frac{\pi}{2b(1+\varepsilon_{yy})}, 0\right)\text{:y-direction} \qquad (8)$$

Yalameha *et al.*

III. RESULTS AND DISCUSSIONS

### III. A. Geometrical structures and stability in the equilibrium state

TiNI monolayer crystallizes in an orthorhombic structure with the space group Pmmn, D_{2h}^{13}, (No. 59), as shown in Fig. 1(a-b). Our calculated lattice constants and atomic positions agree with those reported in the literature (see Table I) [28].

To confirm the dynamical stability of the TiNI monolayer at its equilibrium lattice parameters, we calculated its phonon spectrum, which is shown in Fig. 1(c). The figure demonstrates that all branches have positive frequencies, and there are no imaginary phonon modes throughout the Brillouin zone, indicating the dynamic stability of the TiNI monolayer. Additionally, we plotted the phonon partial density of states (PDOS) in the same figure. The lower frequency DOS is mainly contributed by Ti, while the higher frequency DOS is primarily due to N and I. It is important to note that the mechanical and thermal stability of this monolayer at equilibrium has also been examined by Lei et al. [44].

Table I. Lattice constants and distance between adjacent atoms of TiNI monolayer compared.

	a (Å)	b (Å)	Ti-Ti (Å)	Ti-I (Å)	Ti-N (Å)	N-N (Å)	N-I (Å)	I-I (Å)	I-Ti (Å)
This work	3.537	3.972	2.996	2.836	2.019	2.732	3.227	3.537	2.836
Other work	3.529[a], 3.53[b] 3.51[c]	4.004[a], 3.99[b] 3.98[c]	2.990[a]	2.840[a]	2.030[a]	2.760[a]	3.240[a]	3.530[a]	2.840[a]

[a] Ref. [31], [b] Ref. [26]. [c] Ref. [44]

Yalameha *et al.*

(a)

(b)

-$\overline{X}$ $\overline{\Gamma}$ $\overline{X}$

1D BZ

Y   M K_y

K_x

Γ X

2D BZ

(c)
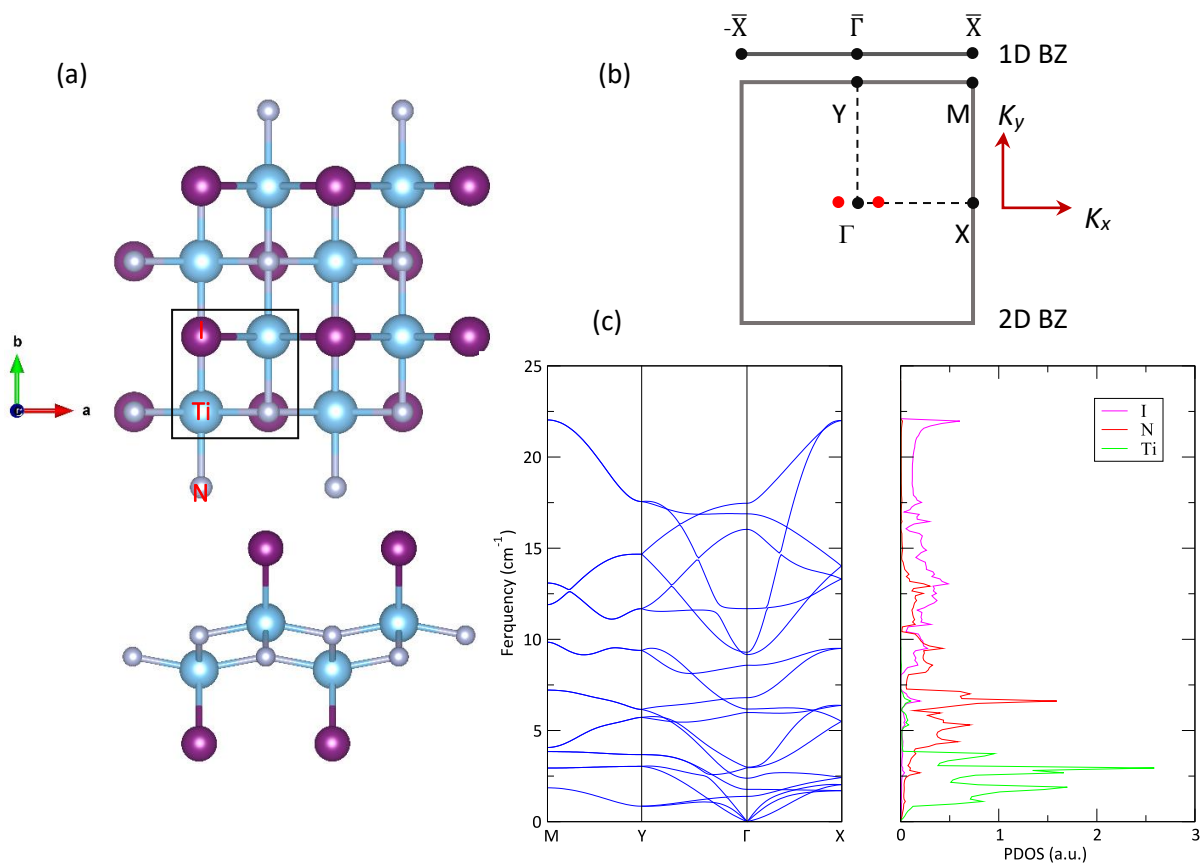
Fig. 1. (a) Top and side views of the crystal structure of the TiNI monolayer; the unit cell is indicated with a solid black square. **(b)** 2D and 1D BZ with specific symmetry points. The red dots represent Dirac points located at $P = (k_x = \pm 0.045, k_y = 0.0)$ Å^{-1} in the 2D BZ. **(c)** Phonon dispersion and PDOS of the TiNI monolayer at its equilibrium lattice parmeters. All the branches have positive frequencies without any imaginary phonon modes in the entire BZ, evidencing the dynamic stability of this monolayer.

Yalameha *et al.*

III. B. Electronic and topological proprieties

At first, we investigate the topological properties and the band inversion of the TiNi monolayer in an equilibrium state within the PBE-GGA approach and compare the results with the previous study [28] (band inversion concept and the factors affecting it are reviewed in the Supplemental Materials). We then revisit these studies within the HSE06 approach in an equilibrium state and under external strains. Also, the dynamical stability of this monolayer is determined under such strains. It should be noted that the study conducted within the PBE-GGA approach is only for an examination of the accuracy of the method and to show why the previous results [28] contradict this work; otherwise, as we will show using the more accurate method based on HSE06, this monolayer cannot be a candidate for the QSH effect at room temperature.
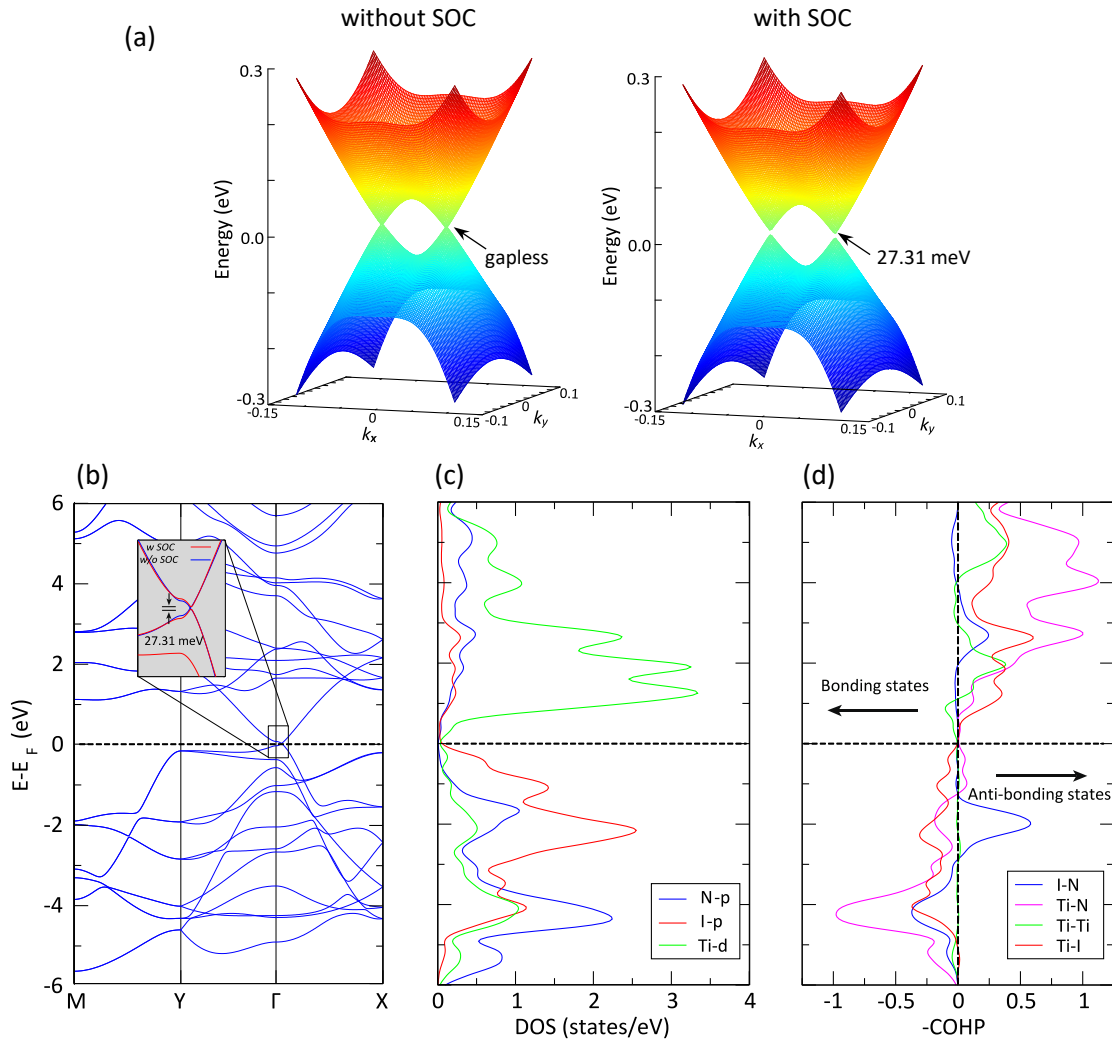
Fig. 2. (a) The 3D electronic band structures of TiNI monolayer using PBE-GGA scheme in the presence and absence of SOC. Without including SOC, TiNI monolayer is gapless. The inclusion of SOC opens up a band gap of 27.31 meV, which is due to the presence of the heavy element iodine. **(b)** The calculated band structures without SOC at high symmetry point. The inset shows the band structure around the Γ point with (red color) and without (blue color) SOC. **(c)** Electron partial density of states (DOS) projected onto different atoms and orbitals of the TiNI monolayer. **(d)** The crystal orbital Hamiltonian populations (COHP) diagram. The negative and positive values of COHP indicate anti-bonding and bonding states, respectively.

Yalameha *et al.*

The 3D electronic band structures of TiNI were calculated employing the PBE-GGA functional in the presence and absence of SOC, as shown in Fig. 2(a, b). Without including SOC, the TiNI monolayer is gapless, showing a semimetallic character with the Dirac-like states slightly away from the Γ point along the Γ-*X* direction (this direction is also shown in Fig. 2(b)). These Dirac-like gapless points are located at $P = (k_x = \pm 0.045, k_y = 0.0)$ Å^{-1} in the 2D BZ (Fig. 1(b)). Considering the SOC, TiNI appears to be an insulator with a small bandgap of 27.31 meV. Nevertheless, this bandgap is significantly smaller than the previous report (50.1 eV) [28]. This difference may be due to minor differences in the lattice constants taken in these two works (see Table I) or the computational code used to perform the calculations as the VASP package (with pseudopotential method) was used in [28], whereas we used WIEN2K (with the full potential method). The calculated partial DOS for N-*p*, I-*p*, and Ti-*d* orbitals are shown in Fig. 2(c) (the other orbitals are neglected due to their small contributions around the Fermi energy). The results show that N-*p* and I-*p* orbitals are occupied below the Fermi energy (E_F), forming 3- and 1- anionic valent states, respectively, while the bands above E_F are mainly dominated by Ti's 3*d* orbitals, making it behave as a 4+ cation. Moreover, the (N-*p*, I-*p*) and (N-*p*, Ti-*d*) states have hybridization around E_F. The calculated COHP of I-N, Ti-N, Ti-Ti, and Ti-I chemical bonds are shown in Fig. 2(d). The negative and positive values of COHP indicate anti-bonding and bonding states, respectively. The anti-bonding states of I-N and Ti-N bands are below E_F (range from 0 to -3.5 eV). The bonding states just above the E_F are derived from Ti-Ti and I-N.

First, to identify the topological nature of this monolayer, we investigate the band inversion. As mentioned earlier, other mechanisms may also lead to band inversion besides SOC. The orbital-resolved band dispersions near the Fermi level using PBE-GGA approach without and with SOC are shown in Fig. 3. According to this figure, the CB and VB around the Γ-point are mainly contributed by the I-p_y and Ti-d_{xy} orbitals, respectively, indicating the band inversion around the Γ point is not due to the SOC (see Fig. 3(a)). The band inversion of this monolayer is due to the hybridization of N-*p* orbitals with I-*p* and Ti-*d* orbitals, as well as the presence of N-I and Ti-Ti bonding states above E_F and the anti-bonding states of Ti-N below E_F. The band inversion can be attributed to the presence of these bonding and anti-bonding states. In addition, this is a typical band inversion between states of opposite parity, insensitive to the presence or absence of SOC, as shown in Fig. 3(a) and (b). Therefore, although the SOC opens the bandgap, it is not playing a defining role in the band inversion. Although the mechanism of band inversion has not been investigated in ref [28], the p_y-d_{xy} band inversion reported there agrees with our results.

The effect of the Hubbard parameter (U) value of 1.2 eV in the GGA+U method was also investigated to understand the topological band order of this monolayer, considering the presence of the Ti element. Fig. 3(d) presents the band structure at the equilibrium state of this monolayer with SOC, obtained using both the GGA and GGA+U approaches, allowing for a direct comparison between the two. Interestingly, in the GGA+U method, band inversion also occurs, with the only difference being a reduction in the bandgap to 15 meV when compared to the GGA method. This result is consistent with previous GGA+U calculations (U = 1 eV) reported by Wang et al. [28].

Yalameha *et al.*

        To confirm the topological features of TiNI, other influential characteristics, namely Wannier Charge Centers (WCCs), are calculated in the absence and presence of SOC. Fig. 3(c) shows the evolution of the WCCs using the Wilson-loop method along the k_x direction in the half of the first BZ. The WCC is crossed at an odd number of times with any straight horizontal line (blue line), revealing that TiNI monolayer is topologically nontrivial (*i.e.*, QSH insulator) with $\mathbb{Z}_2$ = 1. This calculated $\mathbb{Z}_2$ topological index agrees with the results of Ref. [28] (Fu and Kane method [45].) and Ref. [44] (Wilson-loop method).

The emergence of the topological edge states at the boundaries is one of the most characteristic features of nontrivial topological 2D materials. These edge states can be deduced from the bulk-boundary correspondence [46], which indicates that for nontrivial topological invariants, there are gapless surface modes despite the insulating bulk behavior away from the surface. We have calculated the 1D edge states to demonstrate their existence in the TiNI monolayer. Fig. 4 shows the local density of states (LDOS) of the edge states.

        In these calculations, the ribbon width is set to 121.1 Å to avoid the interaction between the two edges, as shown in Fig. 4(a). When the SOC is ignored, there are two edge states (two
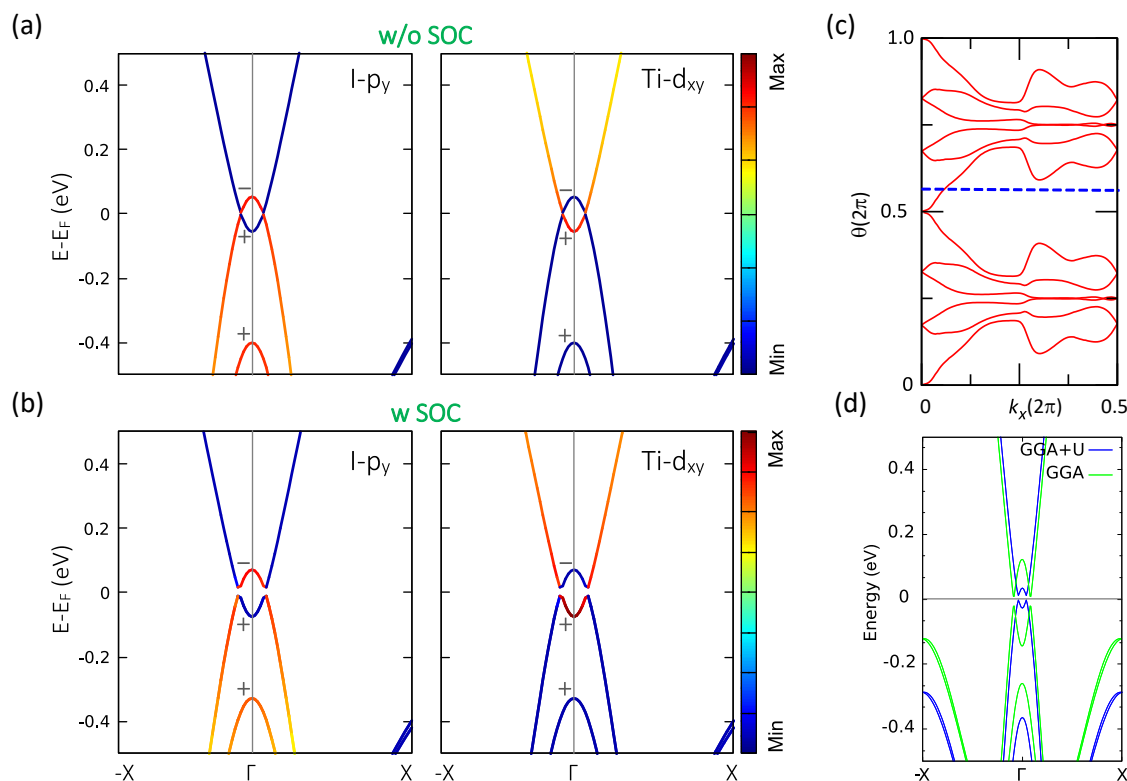

Fig. 3. The I-p_y and Ti-d_{xy} orbital-resolved band dispersions of TiNI monolayer near the Fermi energy without **(a)** and with **(b)** SOC. The CB and VB around the Γ point are mainly formed by the I-p_y and Ti-d_{xy} orbitals, respectively, indicating the band inversion around the Γ point. The parities of the eigenstates at the Γ point are shown with "+" and "−". **(c)** The evolution of WCCs in the presence of SOC. $\mathbb{Z}_2$ index can be obtained by counting the number of times an arbitrary horizontal reference line (blue dash-line) crossed the evolution of the WCCs. $\mathbb{Z}_2$ = 0 for an even and $\mathbb{Z}_2$ = 1 for an odd number of crossings. **(d)** Calculated PBE-GGA (green color) and GGA+U (blue color) band structure of TiNI monolayer with SOC in the equilibrium state. The Hubbard parameter (U) for Ti element has a value of 1.2 eV.

Yalameha *et al.*

(a)
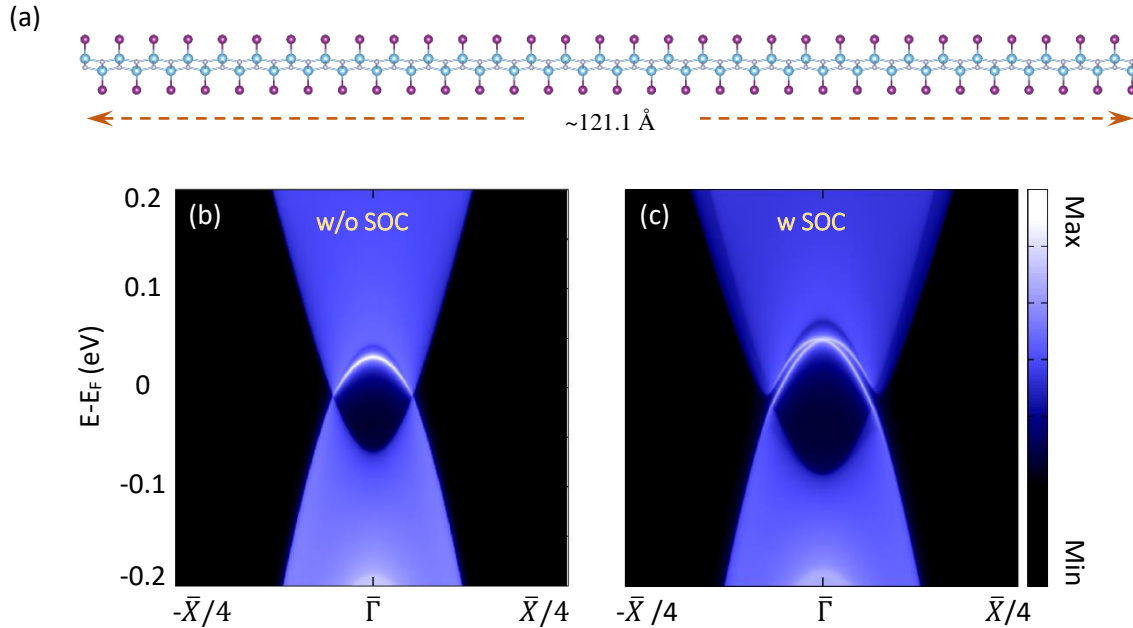
~121.1 Å

Fig. 4. (a) The nanoribbon width is set to 121.1 Å to avoid the interaction between the edges. The local density of states without **(b)** and with **(c)** SOC inclusion. In the absence of the SOC, there are two topological edge states (two branches of the edge states overlap) connecting two 2D Dirac semimetals along the high symmetry line $-\bar{X}$-$\bar{\Gamma}$-$\bar{X}$. With the inclusion of the SOC, the two branches of the topological edge states split due to the energy gap opening, connecting the valence and conduction bands.

branches of the edge states overlap) connecting two 2D Dirac semimetals along the high symmetry line (see 1D BZ projected from 2D BZ in Fig. 2(b)) $-\bar{X}$-$\bar{\Gamma}$ (or $\bar{\Gamma}$-$\bar{X}$), as indicated in Fig. 4(b). In the presence of the SOC hybridization, a narrow bandgap opens, and the edge states split into two branches connecting CB to VB, as shown in Fig. 4(c). The calculated LDOS of the edge states is approximately consistent with the calculated electronic structure of the TiNI nanoribbon in the presence of SOC reported in Ref. [28].

In order to accurately determine the electronic band splitting and investigate the effect of external strain on the band structure and its topological properties, we employed the HSE06 and PBE0 hybrid functionals, as well as the TB-mBJ approaches. We have employed an in-plane uniaxial strain along the *x*- and *y*-axis, maintaining the crystal symmetry by uniformly changing the lattice as $\varepsilon = (l-l_0)/l_0$, where l (l_0) is strained (equilibrium) lattice constants ($l = a$, b). Fig. 5 shows the bandgap variation at the Γ point of the TiNI monolayer under uniaxial strain ($-6 \leq \varepsilon_{x/y} \leq 6\%$) along the *x*-axis and *y*-axis in the presence of SOC within the HSE06 approach. In the equilibrium state (*i.e.*, 0% strain), a trivial bandgap ~ 0.36 eV (~ 0.48 eV) opens in the presence (absence) of SOC. These results are in good agreement with those reported by Liang *et al.* (0.44 eV in the absence of SOC) [26] but contradict the stated 273.1 meV nontrivial bandgap in Ref. [28]. As the uniaxial compression strain increases along the *x*-axis, the trivial bandgap decreases until a critical stress value $\varepsilon_x \approx$ -4% is reached. By passing this critical value, the nontrivial bandgap opens, and the topological phase transition occurs (the band inversion occurs), as shown in Figs. 5(a) and (c). In this case ($\varepsilon_x >$ -4%), the topological properties of this monolayer within the HSE06 approach are similar to corresponding results within the PBE-GGA approach.

Yalameha *et al.*
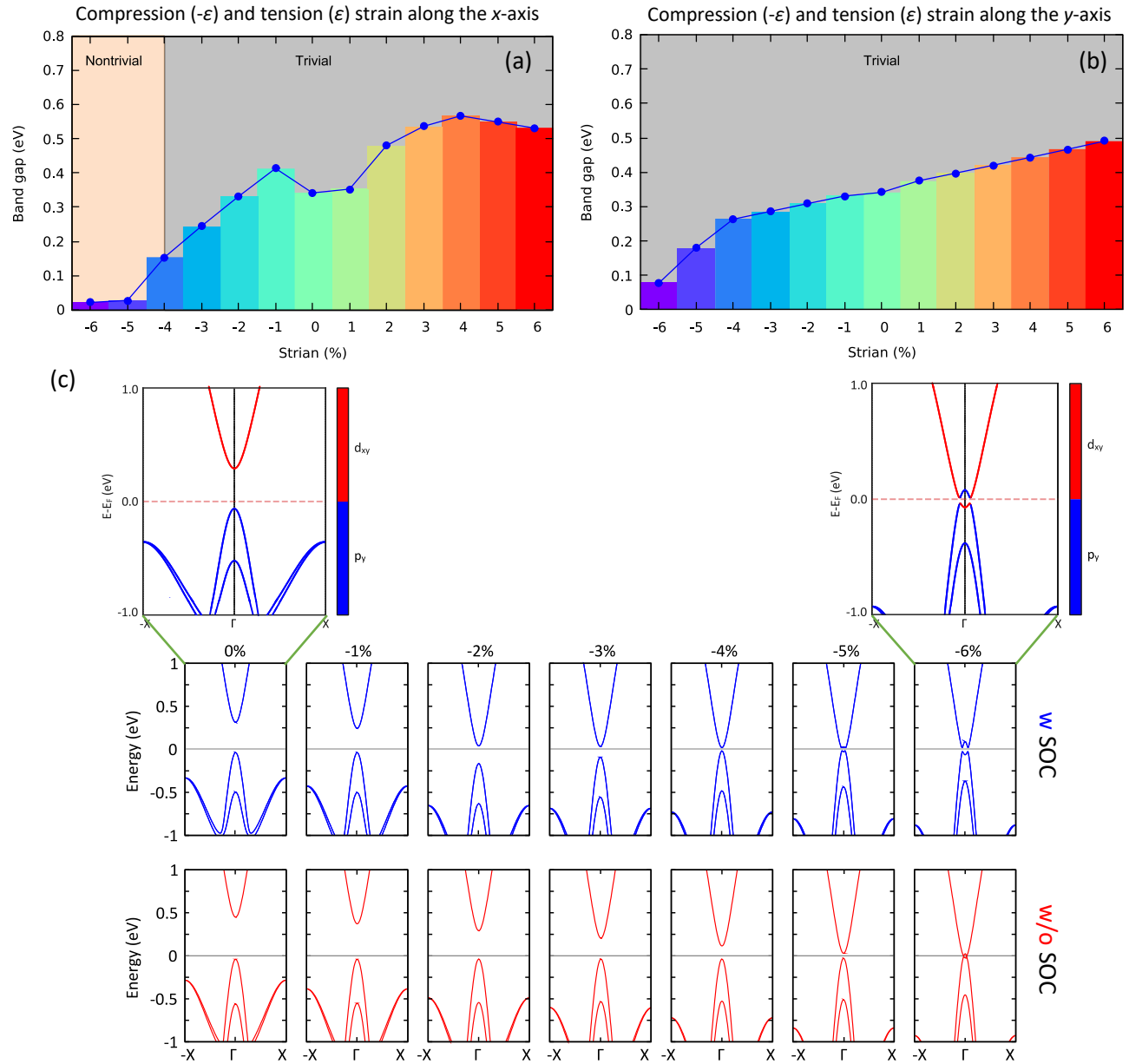
**Fig. 5**. The variation of the bandgap at the Γ point of the TiNI monolayer under uniaxial strain ($-6 \leq \varepsilon_{x/y} \leq 6\%$) along the *x*-axis **(a)** and *y*-axis **(b)** in the presence of SOC within the HSE06 approach. **(c)** Band structures of the TiNI monolayer under the external uniaxial compression strains along the *x*-axis without and with SOC. To correct the electronic structure states, we employed the HSE06 approach. When the SOC effect is not considered, the energy band gap gradually decreases with decreasing lattice constant (a_0), and when it reaches -6%, the bandgap closes. In this case, like the PBE-GGA approach, the band structure shows a semimetallic character with the Dirac semimetal points slightly away from the Γ point along the -X-Γ-X direction. Considering the SOC simultaneously, a nontrivial band gap opens. The I-p_y and Ti-d_{xy} orbital-resolved band dispersions within the HSE06 approach of TiNI monolayer near E_F with SOC for -0% and -6% are calculated.

In the case of uniaxial compression strains along the y-axis, the bandgap value decreases gradually and linearly relative to the strain, and the topological phase transition does not occur, as

Yalameha *et al.*

demonstrated in Fig. 5(b) (detailed band structure information is available in the Supplemental materials).

We also investigated the bandgap variation at the Γ point of this monolayer under uniaxial strains along the *x*-axis and *y*-axis in the presence and absence of SOC within the PBE0 approach (see Figs. S5 and S6). The calculated bandgap in the equilibrium state for the TiNI monolayer using the PBE0 functional is 0.95 eV (with SOC) and 1.08 eV (without SOC). The different results obtained using PBE0 compared to HSE06 may stem from the fact that the exchange energy for HSE06 has less Hartree-Fock fraction than PBE0 [34, 47]. However, band inversion does not occur in this approach under different uniaxial strains. Phonon dispersion calculations show that TiNI monolayer under uniaxial compression strains along the *x*-axis maintains its dynamic stability up to a maximum of -1% to -3%, and in the strains $\varepsilon_x > -3\%$, negative frequency modes appear in the phonon dispersion (see Fig. S7). Therefore, although this monolayer transitions to a nontrivial topological phase under strains $\varepsilon_x > -4\%$ along the *x*-axis, it cannot find practical applications due to its instability unless the material is somehow stabilized, e.g., using doping.
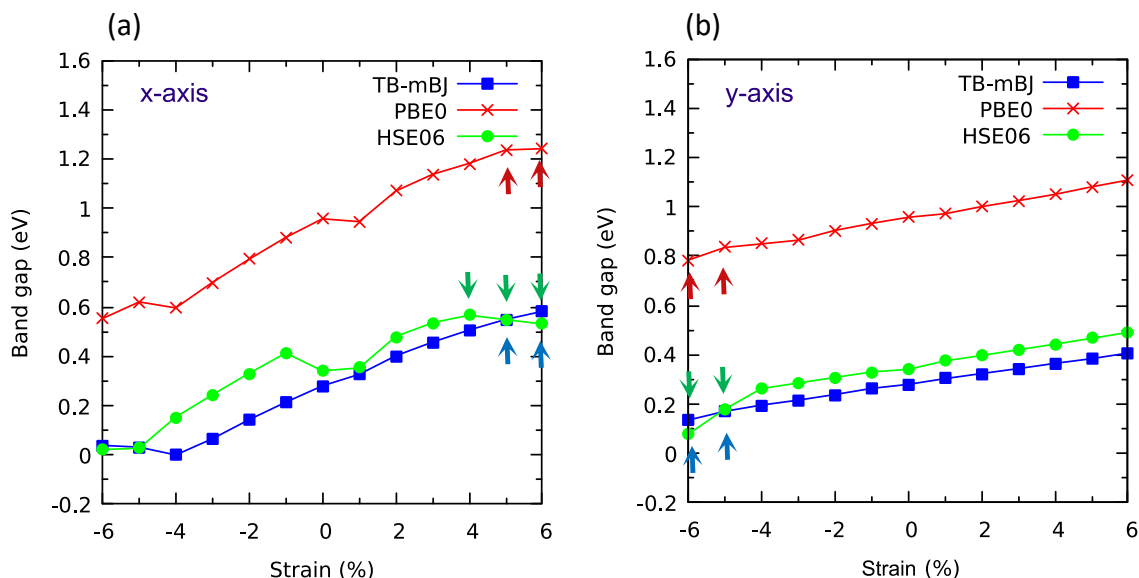
Fig. 6. The variation of the bandgap of the TiNI monolayer under uniaxial strain (-6% to 6%) along the **(a)** *x*-axis and **(b)** *y*-axis. Three approaches (HSE06, PBE0, and TB-mBJ) were used to analyze the changes in the bandgap. Colored arrows indicate indirect band gaps (Γ → X).

In addition to the hybrid functionals discussed earlier, the TB-mBJ approach was also employed to investigate the electronic and topological properties of the TiNI monolayer. The TB-mBJ calculations revealed that, in its equilibrium state, the TiNI monolayer possesses a trivial band gap of 281 meV with SOC. The band structures of the TiNI monolayer under external uniaxial strains along the x- and y-axis with SOC were also investigated and are presented in Fig. S9 in the supplementary materials. As shown in Fig. S9(a), when the uniaxial compression strain along the x-axis reaches $\varepsilon_x = -4\%$, the band gap becomes zero, marking the topological phase transition point. Beyond this critical point, band inversion occurs, and a nontrivial bandgap of approximately 31 meV emerges. When subjected to tensile strain along the x-axis (or compressive strain along the

Yalameha *et al.*

y-axis), the TiNI monolayer exhibits an increase (or decrease) in its bandgap, resulting in a transition from a trivial bandgap to an indirect bandgap ($\Gamma \rightarrow X$) (Fig. S9(b) and (c)). On the other hand, when subjected to tensile strain along the y-axis, the bandgap gradually and linearly increases (Fig. S9(d)).

Finally, to compare the effect of strain on the band gap in HSE06, PBE0 and TB-mBJ approaches, the variations of the bandgap as a function of strain in the *x*- and *y*-axis are specified in Fig. 6. Fig. 6(a) illustrates that, for the strains ranging from -6% to 6% along the *x*-axis, there is an increasing trend in the band gap demonstrated by all three approaches. As indicated by the arrows in this figure, a strain level above 5% leads to a transformation of the direct band gap into an indirect one. As can be seen in Fig. 6(b), the bandgap increases linearly with the increase of uniaxial tensile strain. This trend is also linear for uniaxial compression strains and the bandgap decreases with increasing strain. At uniaxial compressive strains above -5%, the direct bandgap turns into an indirect bandgap. The results show that the bandgap calculated by two approaches TB-mBJ and HSE06 are very close to each other, while PBE0 approach shows the bandgap with larger values. This is because it has been found that PBE0 tends to overestimate the band gaps. [48]. It has been found that for band gaps smaller than 5.0 eV, the HSE06 hybrid functional leads to results that are rather close to the experimental values, however, there is a clear underestimation for large band gaps [49]. Moreover, TB-mBJ approach is the most balanced potential, not showing obvious underestimation or overestimation for small or large band gaps [31, 49]. Therefore, at the moment the TB-mBJ approach represents the best alternative to the much more expensive hybrid functional method such as PBE0 and HSE06 approaches.

IV. Conclusions

In conclusion, our first-principles calculations demonstrate that the electronic structure and topological properties of the TiNI monolayer are highly dependent on the choice of functional used for the calculation. While the PBE-GGA approach exhibits band inversion in both the presence and absence of spin-orbit coupling [28], our more accurate band structure analyses within the HSE06, PBE0, and TB-mBJ approaches show that no band inversion occurs in the equilibrium state. On the other hand, the GGA+U method exhibits band inversion as well, with the only difference being a decrease in the bandgap to 15 meV compared to the PBE-GGA approach. Our findings further reveal that under compression strain within the HSE06 and TB-mBJ approaches, the band inversion occurs similarly to the PBE-GGA approach, but the monolayer becomes dynamically unstable. These results contradict the findings of a previous study and demonstrate that the TiNI monolayer cannot play a role as a quantum spin Hall system in practical applications.

Furthermore, our findings highlight the potential pitfalls of relying solely on general-purpose functionals such as PBE-GGA or GGA+U when studying 2D or 3D topological insulators. These functionals can result in false predictions and mislead experimentalists in their effort to grow new TIs. While these functionals are designed to be relatively simple and computationally efficient, they do not always accurately capture the complex electronic behavior of TIs. Overall, our study provides valuable insights into the electronic properties and topological behavior of TiNI

Yalameha *et al.*

monolayer, contributing to the growing body of knowledge on 2D materials and topological insulators.

V. References

1. Ren, Y., Z. Qiao, and Q. Niu, *Topological phases in two-dimensional materials: a review.* Reports on Progress in Physics, 2016. **79**(6): p. 066501.
2. Polash, M.M.H., et al., *Topological quantum matter to topological phase conversion: Fundamentals, materials, physical systems for phase conversions, and device applications.* Materials Science and Engineering: R: Reports, 2021. **145**: p. 100620.
3. Hasan, M.Z. and C.L. Kane, *Colloquium: topological insulators.* Reviews of modern physics, 2010. **82**(4): p. 3045.
4. Moore, J.E. and L. Balents, *Topological invariants of time-reversal-invariant band structures.* Physical Review B, 2007. **75**(12): p. 121306.
5. Bernevig, B.A., T.L. Hughes, and S.-C. Zhang, *Quantum spin Hall effect and topological phase transition in HgTe quantum wells.* science, 2006. **314**(5806): p. 1757-1761.
6. Jin, Y., et al., *Two-Dimensional Dirac Semimetals without Inversion Symmetry.* Physical Review Letters, 2020. **125**(11): p. 116402.
7. Narimani, M., S. Yalameha, and Z. Nourbakhsh, *High thermoelectric efficiency of LaX (X= Sb, Bi) two dimensional topological insulators.* Journal of Physics: Condensed Matter, 2020. **32**(25): p. 255501.
8. Yan, B. and S.-C. Zhang, *Topological materials.* Reports on Progress in Physics, 2012. **75**(9): p. 096501.
9. Zhou, L., et al., *New family of quantum spin Hall insulators in two-dimensional transition-metal halide with large nontrivial band gaps.* Nano letters, 2015. **15**(12): p. 7867-7872.
10. Novoselov, K.S., et al., *Two-dimensional gas of massless Dirac fermions in graphene.* nature, 2005. **438**(7065): p. 197-200.
11. Nie, Y., et al., *First-principles design of a Dirac semimetal: An NP monolayer.* Physical Review B, 2020. **101**(23): p. 235443.
12. Ma, Y., Y. Jing, and T. Heine, *Double Dirac point semimetal in 2D material: Ta2Se3.* 2D Materials, 2017. **4**(2): p. 025111.
13. Wang, B., et al., *A new Dirac cone material: a graphene-like Be 3 C 2 monolayer.* Nanoscale, 2017. **9**(17): p. 5577-5582.
14. Zhao, Y., et al., *A new anisotropic dirac cone material: a b2s honeycomb monolayer.* The Journal of Physical Chemistry Letters, 2018. **9**(7): p. 1815-1820.
15. Zhang, W., et al., *First-principles studies of the three-dimensional strong topological insulators Bi2Te3, Bi2Se3 and Sb2Te3.* New Journal of Physics, 2010. **12**(6): p. 065013.
16. Zhang, H., et al., *Topological insulators in Bi 2 Se 3, Bi 2 Te 3 and Sb 2 Te 3 with a single Dirac cone on the surface.* Nature physics, 2009. **5**(6): p. 438-442.
17. Parveen, A., et al., *Correction: Topological behaviour of ternary non-symmorphic crystals KZnX (X= P, As, Sb) under pressure and strain: a first principles study.* Physical Chemistry Chemical Physics, 2018. **20**(39): p. 25548-25550.
18. Kane, C.L. and E.J. Mele, *Z 2 topological order and the quantum spin Hall effect.* Physical review letters, 2005. **95**(14): p. 146802.
19. Ortmann, F., S. Roche, and S.O. Valenzuela, *Topological insulators: Fundamentals and perspectives.* 2015: John Wiley & Sons.
20. Jung, Y., J. Shen, and J.J. Cha, *Surface effects on electronic transport of 2D chalcogenide thin films and nanostructures.* Nano Convergence, 2014. **1**(1): p. 1-8.
21. Wilczek, F., *Majorana returns.* Nature Physics, 2009. **5**(9): p. 614-618.
22. Qi, X.-L., et al., *Inducing a magnetic monopole with topological surface states.* science, 2009. **323**(5918): p. 1184-1187.

Yalameha *et al.*

23. Pesin, D. and A.H. MacDonald, *Spintronics and pseudospintronics in graphene and topological insulators.* Nature materials, 2012. **11**(5): p. 409-416.
24. Garate, I. and M. Franz, *Inverse spin-galvanic effect in the interface between a topological insulator and a ferromagnet.* Physical review letters, 2010. **104**(14): p. 146802.
25. Juza, R. and J. Heners, *Über nitridhalogenide des titans und zirkons.* Zeitschrift für anorganische und allgemeine Chemie, 1964. **332**(3-4): p. 159-172.
26. Liang, Y., et al., *Novel titanium nitride halide TiNX (X= F, Cl, Br) monolayers: potential materials for highly efficient excitonic solar cells.* Journal of Materials Chemistry A, 2018. **6**(5): p. 2073-2080.
27. Schurz, C.M., et al., *Superconducting nitride halides MNX (M= Ti, Zr, Hf; X= Cl, Br, I).* 2011.
28. Wang, A., et al., *Band inversion and topological aspects in a TiNI monolayer.* Physical Chemistry Chemical Physics, 2016. **18**(32): p. 22154-22159.
29. Wang, C. and G. Gao, *Titanium nitride halides monolayers: promising 2D anisotropic thermoelectric materials.* Journal of Physics: Condensed Matter, 2020. **32**(20): p. 205503.
30. Gresch, D., et al., *Z2Pack: Numerical implementation of hybrid Wannier centers for identifying topological materials.* Physical Review B, 2017. **95**(7): p. 075146.
31. Blaha, P., et al., *WIEN2k: An APW+ lo program for calculating the properties of solids.* The Journal of Chemical Physics, 2020. **152**(7): p. 074101.
32. Perdew, J.P., K. Burke, and M. Ernzerhof, *Generalized gradient approximation made simple.* Physical review letters, 1996. **77**(18): p. 3865.
33. Heyd, J., G.E. Scuseria, and M. Ernzerhof, *Hybrid functionals based on a screened Coulomb potential.* The Journal of chemical physics, 2003. **118**(18): p. 8207-8215.
34. Adamo, C., G.E. Scuseria, and V. Barone, *Accurate excitation energies from time-dependent density functional theory: Assessing the PBE0 model.* The Journal of chemical physics, 1999. **111**(7): p. 2889-2899.
35. Headspith, D.A. and M.G. Francesconi, *Transition metal pnictide-halides: A class of under-explored compounds.* Topics in Catalysis, 2009. **52**: p. 1611-1627.
36. Jiang, H., *Band gaps from the Tran-Blaha modified Becke-Johnson approach: A systematic investigation.* The Journal of chemical physics, 2013. **138**(13): p. 134115.
37. Sancho, M.L., et al., *Highly convergent schemes for the calculation of bulk and surface Green functions.* Journal of Physics F: Metal Physics, 1985. **15**(4): p. 851.
38. Tillack, S., A. Gulans, and C. Draxl, *Maximally localized Wannier functions within the (L) APW+ LO method.* Physical Review B, 2020. **101**(23): p. 235102.
39. Pizzi, G., et al., *Wannier90 as a community code: new features and applications.* Journal of Physics: Condensed Matter, 2020. **32**(16): p. 165902.
40. Yu, R., et al., *Equivalent expression of Z2 topological invariant for band insulators using the non-Abelian Berry connection.* Physical Review B, 2011. **84**(7): p. 075119.
41. Yalameha, S., Z. Nourbakhsh, and A. Vaez, *Hydrostatic strain-induced topological phase of KNa2Sb.* Journal of Magnetism and Magnetic Materials, 2018. **468**: p. 279-286.
42. Togo, A., F. Oba, and I. Tanaka, *First-principles calculations of the ferroelastic transition between rutile-type and CaCl 2-type SiO 2 at high pressures.* Physical Review B, 2008. **78**(13): p. 134106.
43. Nelson, R., et al., *LOBSTER: Local orbital projections, atomic charges, and chemical-bonding analysis from projector-augmented-wave-based density-functional theory.* Journal of Computational Chemistry, 2020.
44. Lei, W., et al., *The TiNI monolayer: a two-dimensional system with promising ferroelastic, topological, and thermoelectric properties.* Physical Chemistry Chemical Physics, 2022. **24**(46): p. 28134-28140.
45. Fu, L. and C.L. Kane, *Topological insulators with inversion symmetry.* Physical Review B, 2007. **76**(4): p. 045302.
46. Franz, M. and L. Molenkamp, *Topological insulators*. 2013: Elsevier.

47. Jaramillo, J., G.E. Scuseria, and M. Ernzerhof, *Local hybrid functionals.* The Journal of chemical physics, 2003. **118**(3): p. 1068-1073.
48. Garza, A.J. and G.E. Scuseria, *Predicting band gaps with hybrid density functionals.* The journal of physical chemistry letters, 2016. **7**(20): p. 4165-4170.
49. Tran, F. and P. Blaha, *Importance of the kinetic energy density for band gap calculations in solids with density functional theory.* The Journal of Physical Chemistry A, 2017. **121**(17): p. 3318-3325.